Biomedical Optics EXPRESS

Wide field-of-view fluorescence image deconvolution with aberration-estimation from Fourier ptychography

Jaebum Chung,[1,*] Jinho Kim,[1] Xiaoze Ou,[1] Roarke Horstmeyer,[1] and Changhuei Yang[1]

[1]*Department of Electrical Engineering, California Institute of Technology, Pasadena, CA 91125, USA*
[*]*jchung@caltech.edu*

Abstract: This paper presents a method to simultaneously acquire an aberration-corrected, wide field-of-view fluorescence image and a high-resolution coherent bright-field image using a computational microscopy method. First, the procedure applies Fourier ptychographic microscopy (FPM) to retrieve the amplitude and phase of a sample, at a resolution that significantly exceeds the cutoff spatial frequency of the microscope objective lens. At the same time, redundancy within the set of acquired FPM bright-field images offers a means to estimate microscope aberrations. Second, the procedure acquires an aberrated fluorescence image, and computationally improves its resolution through deconvolution with the estimated aberration map. An experimental demonstration successfully improves the bright-field resolution of fixed, stained and fluorescently tagged HeLa cells by a factor of 4.9, and reduces the error caused by aberrations in a fluorescence image by up to 31%, over a field of view of 6.2 mm by 9.3 mm. For optimal deconvolution, we show the fluorescence image needs to have a signal-to-noise ratio of at least ~18.

OCIS codes: (180.2520) Fluorescence microscopy; (070.0070) Fourier optics and signal processing.

References and links

1. J. W. Lichtman and J.-A. Conchello, "Fluorescence microscopy," Nat. Methods **2**(12), 910–919 (2005).
2. E. Kissa, *Dispersions: Characterization, Testing, and Measurement* (Marcel Dekker, Inc, 1999).
3. D. J. Stephens and V. J. Allan, "Light microscopy techniques for live cell imaging," Science **300**(5616), 82–86 (2003).
4. A. R. Kherlopian, T. Song, Q. Duan, M. A. Neimark, M. J. Po, J. K. Gohagan, and A. F. Laine, "A review of imaging techniques for systems biology," BMC Syst. Biol. **2**(1), 74 (2008).
5. G. Zheng, R. Horstmeyer, and C. Yang, "Wide-field, high-resolution Fourier ptychographic microscopy," Nat. Photonics **7**(9), 739–745 (2013).
6. X. Ou, R. Horstmeyer, C. Yang, and G. Zheng, "Quantitative phase imaging via Fourier ptychographic microscopy," Opt. Lett. **38**(22), 4845–4848 (2013).
7. X. Ou, G. Zheng, and C. Yang, "Embedded pupil function recovery for Fourier ptychographic microscopy," Opt. Express **22**(5), 4960–4972 (2014).
8. R. Kingslake and R. B. Johnson, *Lens Design Fundamentals*, 2nd ed. (SPIE Press, 2010).
9. S. Dong, K. Guo, P. Nanda, R. Shiradkar, and G. Zheng, "FPscope: a field-portable high-resolution microscope using a cellphone lens," Biomed. Opt. Express **5**(10), 3305–3310 (2014).
10. K. Guo, S. Dong, P. Nanda, and G. Zheng, "Optimization of sampling pattern and the design of Fourier ptychographic illuminator," Opt. Express **23**(5), 6171–6180 (2015).
11. S. Dong, R. Shiradkar, P. Nanda, and G. Zheng, "Spectral multiplexing and coherent-state decomposition in Fourier ptychographic imaging," Biomed. Opt. Express **5**(6), 1757–1767 (2014).
12. L. Tian, X. Li, K. Ramchandran, and L. Waller, "Multiplexed coded illumination for Fourier Ptychography with an LED array microscope," Biomed. Opt. Express **5**(7), 2376–2389 (2014).
13. A. Williams, J. Chung, X. Ou, G. Zheng, S. Rawal, Z. Ao, R. Datar, C. Yang, and R. Cote, "Fourier ptychographic microscopy for filtration-based circulating tumor cell enumeration and analysis," J. Biomed. Opt. **19**(6), 066007 (2014).

#252832 Received 2 Nov 2015; revised 16 Dec 2015; accepted 29 Dec 2015; published 7 Jan 2016

14. G. Zheng, X. Ou, R. Horstmeyer, and C. Yang, "Characterization of spatially varying aberrations for wide field-of-view microscopy," Opt. Express **21**(13), 15131–15143 (2013).
15. S. Dong, P. Nanda, R. Shiradkar, K. Guo, and G. Zheng, "High-resolution fluorescence imaging via pattern-illuminated Fourier ptychography," Opt. Express **22**(17), 20856–20870 (2014).
16. C. Pask, "Simple optical theory of super-resolution," J. Opt. Soc. Am. **66**(1), 68–70 (1976).
17. R. Heintzmann, "Estimating missing information by maximum likelihood deconvolution," Micron **38**(2), 136–144 (2007).
18. J. L. Harris, "Resolving Power and Decision Theory," J. Opt. Soc. Am. **54**(5), 606–609 (1964).
19. D. A. Nahrstedt and L. C. Schooley, "Alternative approach in decision theory as applied to the resolution of two point images," J. Opt. Soc. Am. **69**(6), 910–912 (1979).
20. P. J. Sementilli, B. R. Hunt, and M. S. Nadar, "Analysis of the limit to superresolution in incoherent imaging," J. Opt. Soc. Am. A **10**(11), 2265–2276 (1993).
21. A. J. den Dekker and A. van den Bos, "Resolution: a survey," J. Opt. Soc. Am. A **14**(3), 547–557 (1997).
22. L. G. Leff and A. A. Leff, "Use of green fluorescent protein to monitor survival of genetically engineered bacteria in aquatic environments," Appl. Environ. Microbiol. **62**(9), 3486–3488 (1996).
23. K. G. Porter and Y. S. Feig, "The use of DAPI for identifying and counting aquatic microflora1," Limnol. Oceanogr. **25**(5), 943–948 (1980).
24. C.-C. Liang, A. Y. Park, and J.-L. Guan, "In vitro scratch assay: a convenient and inexpensive method for analysis of cell migration in vitro," Nat. Protoc. **2**(2), 329–333 (2007).
25. T. Schroeder, "Long-term single-cell imaging of mammalian stem cells," Nat. Methods **8**(4S), S30–S35 (2011).
26. R. Horstmeyer and C. Yang, "A phase space model of Fourier ptychographic microscopy," Opt. Express **22**(1), 338–358 (2014).
27. J. R. Fienup, "Phase retrieval algorithms: a comparison," Appl. Opt. **21**(15), 2758–2769 (1982).
28. V. Elser, "Phase retrieval by iterated projections," J. Opt. Soc. Am. A **20**(1), 40–55 (2003).
29. P. Godard, M. Allain, V. Chamard, and J. Rodenburg, "Noise models for low counting rate coherent diffraction imaging," Opt. Express **20**(23), 25914–25934 (2012).
30. C. Yang, J. Qian, A. Schirotzek, F. Maia, and S. Marchesini, "Iterative Algorithms for Ptychographic Phase Retrieval," *http://arxiv.org/abs/1105.5628*.
31. R. Horstmeyer, R. Y. Chen, X. Ou, B. Ames, J. A. Tropp, and C. Yang, "Solving ptychography with a convex relaxation," New J. Phys. **17**(5), 053044 (2015).
32. H. H. Bauschke, P. L. Combettes, and D. R. Luke, "Phase retrieval, error reduction algorithm, and Fienup variants: a view from convex optimization," J. Opt. Soc. Am. A **19**(7), 1334–1345 (2002).
33. Y. Shechtman, Y. C. Eldar, A. Szameit, and M. Segev, "Sparsity based sub-wavelength imaging with partially incoherent light via quadratic compressed sensing," Opt. Express **19**(16), 14807–14822 (2011).
34. L. Tian, Z. Liu, L.-H. Yeh, M. Chen, J. Zhong, and L. Waller, "Computational illumination for high-speed in vitro Fourier ptychographic microscopy," Optica **2**(10), 904–911 (2015).
35. X. Ou, R. Horstmeyer, G. Zheng, and C. Yang, "High numerical aperture Fourier ptychography: principle, implementation and characterization," Opt. Express **23**(3), 3472–3491 (2015).
36. M. Guizar-Sicairos and J. R. Fienup, "Phase retrieval with transverse translation diversity: a nonlinear optimization approach," Opt. Express **16**(10), 7264–7278 (2008).
37. P. Thibault, M. Dierolf, A. Menzel, O. Bunk, C. David, and F. Pfeiffer, "High-Resolution Scanning X-Ray Diffraction Microscopy," Science **321**(5887), 379–382 (2008).
38. P. Thibault, M. Dierolf, O. Bunk, A. Menzel, and F. Pfeiffer, "Probe retrieval in ptychographic coherent diffractive imaging," Ultramicroscopy **109**(4), 338–343 (2009).
39. A. M. Maiden and J. M. Rodenburg, "An improved ptychographical phase retrieval algorithm for diffractive imaging," Ultramicroscopy **109**(10), 1256–1262 (2009).
40. J. W. Goodman, *Introduction to Fourier Optics* (Roberts and Company Publishers, 2004).
41. R. C. Gonzalez and R. E. Woods, *Digital Image Processing* (Prentice Hall, 2002).
42. P. Sarder and A. Nehorai, "Deconvolution methods for 3-D fluorescence microscopy images," IEEE Signal Process. Mag. **23**(3), 32–45 (2006).
43. N. Wiener, *The Extrapolation, Interpolation and Smoothing of Stationary Time Series* (The MIT Press, 1949).
44. J. C. Russ, *The Image Processing Handbook,* Fifth ed. (CRC Press, 2007).
45. M. Bertero and P. Boccacci, *Introduction to Inverse Problems in Imaging* (Taylor & Francis, 1998).
46. G. M. P. Kempen and V. L. J. Vliet, "A quantitative comparison of image restoration methods for confocal microscopy," J. Microsc. **185**(3), 354–365 (1997).
47. G. E. Healey and R. Kondepudy, "Radiometric CCD camera calibration and noise estimation," IEEE Trans. Pattern Anal. Mach. Intell. **16**(3), 267–276 (1994).
48. J. R. Fienup, "Invariant error metrics for image reconstruction," Appl. Opt. **36**(32), 8352–8357 (1997).
49. J. Waters and T. Wittmann, *Quantitative Imaging in Cell Biology: Methods in Cell Biology* (Academic Press, 2014).
50. D. Kundur and D. Hatzinakos, "Blind image deconvolution," IEEE Signal Process. Mag. **13**(3), 43–64 (1996).
51. L. Yuan, J. Sun, L. Quan, and H.-Y. Shum, "Progressive inter-scale and intra-scale non-blind image deconvolution," ACM Trans. Graph. **27**(3), 1–10 (2008).
52. J.-H. Lee and Y.-S. Ho, "High-quality non-blind image deconvolution with adaptive regularization," J. Vis. Commun. Image Represent. **22**(7), 653–663 (2011).

#252832 Received 2 Nov 2015; revised 16 Dec 2015; accepted 29 Dec 2015; published 7 Jan 2016

53. R. P. Perry, "Kinetics of nucleoside incorporation into nuclear and cytoplasmic RNA," J. Biophys. Biochem. Cytol. **11**(1), 1–13 (1961).
54. L. Tian and L. Waller, "3D intensity and phase imaging from light field measurements in an LED array microscope," Optica **2**(2), 104–111 (2015).
55. B. M. Hanser, M. G. Gustafsson, D. A. Agard, and J. W. Sedat, "Phase retrieval for high-numerical-aperture optical systems," Opt. Lett. **28**(10), 801–803 (2003).
56. B. M. Hanser, M. G. Gustafsson, D. A. Agard, and J. W. Sedat, "Phase-retrieved pupil functions in wide-field fluorescence microscopy," J. Microsc. **216**(1), 32–48 (2004).
57. G. R. Brady and J. R. Fienup, "Nonlinear optimization algorithm for retrieving the full complex pupil function," Opt. Express **14**(2), 474–486 (2006).

1. Introduction

Bright-field imaging is one of the most popular microscope modalities. A bright-field microscope typically illuminates a specimen with white light and captures an image of the transmitted light. Bright-field image contrast offers information about sample structure [1]. In combination with phase contrast methods, one may quantitatively measure sample absorption, thickness, and dispersion [2]. Another increasingly important microscope modality in biology is fluorescence imaging. Fluorescence can help visualize chemical compositions and structures at a molecular level through appropriate labeling with fluorophores [3, 4]. By illuminating a tagged sample at the fluorophores' excitation light and imaging at the fluorophores' emission wavelength, biologists can easily identify labeled regions exhibiting chemical properties of interest. Combining a bright-field and fluorescence image allows one to locate fluorescing regions relative to the specimen's underlying structure.

In this paper, we report a method that can simultaneously generate a high-resolution, coherent bright-field image, along with an aberration-corrected fluorescence image, across a wide imaging system field-of-view (FOV). Specifically, we first improve bright-field image resolution using Fourier ptychographic microscopy (FPM), a recently developed computational technique that processes a sequence of images acquired under angularly varying illumination [5]. As a phase retrieval method, FPM also recovers the phase information of the sample [6], and can additionally estimate the imaging system's aberrations [7]. Second, we then capture a fluorescence image using the same microscope setup, and correct its aberrations using the aberration map measured via FPM. Specifically, FPM outputs a complex aberration map in the form of a spatially varying pupil function, with which we compute the microscope's spatially varying incoherent point spread function (PSF) to use in fluorescence image deconvolution for aberration removal.

Due to the limitations of physical lens design, imaging systems tend to exhibit aberrations that vary across their FOV [8]. For wide FOV microscopes (i.e., such as those used for gigapixel imaging via FPM [9–13]), aberrations significantly deteriorate image quality near the FOV boundary. Thus, aberration correction becomes a critical step to consistently resolve sample features across the entire image plane [14]. As demonstrated in prior work [7], the coherent nature of FPM allows us to algorithmically account for the microscope's complex and spatially varying aberrations using a procedure termed embedded pupil function recovery (EPRY). The output of the EPRY algorithm is both a high-resolution estimate of a sample's amplitude and phase (i.e., the same as FPM), along with an estimate of the microscope's pupil function. The same algorithm cannot be directly applied to improve fluorescence imaging because both FPM and EPRY only operate in coherent imaging schemes. Fluorescence is incoherent, so it does not change in response to angularly varying illumination. However, some insights from FPM and EPRY do in fact carry over to improve fluorescence resolution using different illumination schemes [15]. Here, we make use of the insight that the aberrations impacting the fluorescence image can be corrected by using the pupil function determined by EPRY.

The aberration removal procedure involves deconvolution with the associated incoherent PSF using Tikhonov regularization. Since both the coherent bright-field and fluorescence images are acquired from the same microscope in quick succession and without any

#252832 Received 2 Nov 2015; revised 16 Dec 2015; accepted 29 Dec 2015; published 7 Jan 2016

movement, we demonstrate that this direct connection between the pupil function and incoherent PSF is accurate. We note that our deconvolution method is aimed at correcting the aberrations in the fluorescence image caused by imperfections in the imaging system. If done perfectly, it should allow us to render a fluorescence image at the diffraction limit of the system.

This deconvolution is distinct from super-resolution deconvolution methods that can reconstruct information outside the passband by incorporating a-priori knowledge of sample structure (e.g., one consisting only of lines or points [16–19]) or an infinite SNR [20, 21]. Here, we are primarily concerned with imaging unknown biological samples, and thus make no a-priori assumptions about their structures. The combination of aberration-corrected fluorescence image and a high-resolution bright-field image in a large FOV format makes this method potentially suitable for applications, such as counting fluorescently tagged bacteria [22, 23], studying cell migration dynamics [24], and tracing cell lineage [25].

This paper is outlined in the following manner: in section 2, we describe our algorithm for aberration characterization and aberration removal in incoherent imaging. In section 3-4, we demonstrate the implementation of our algorithm in a microscope while imaging a sample of fluorescent beads, as well as a fixed, stained, and fluorescently tagged HeLa cell slide. We show that our approach corrects for spatially varying aberrations to enable accurate, wide-field imaging. In section 5, we quantify how much fluorescence signal must be collected for a successful image deconvolution. Finally, we conclude by discussing the implications of our results.

2. Principle of operation

As noted above, we characterize the aberrations within our microscope setup using both FPM and the EPRY algorithm. Complete descriptions of these two techniques are available in previous publications [5, 7]. Here, we offer a short summary of each. First, FPM begins by capturing a series of low-resolution images under varying plane wave illumination. In this FPM setup, we use an LED array placed at a large distance behind the sample of interest for our angularly varying illumination source. For N different LEDs, we turn on one LED at a time and capture a unique image. For the remainder of this manuscript, we treat the light emitted from each LED as quasi-monochromatic and spatially coherent across the sample area. A detailed discussion of the requirements and impact of source coherence for FPM is in [26].

Assuming the imaged sample is thin, an angularly varying illumination source creates a laterally shifting sample spectrum (i.e., the Fourier transform of the complex sample) in the back-focal plane of the objective lens. At this plane, the finite extent of the objective lens aperture stop (connected to the lens NA) acts as a low-pass filter. In a conventional infinity-corrected microscope objective lens, the extent of the aperture stop defines its cutoff spatial frequency, which in turn dictates its smallest resolvable feature at the image plane. By laterally shifting the sample spectrum via varied LED illumination and acquiring a sequence of limited resolution images, FPM acquires a data set that contains sufficient information to reconstruct an image with a wider spectrum than offered by a single image.

However, since the sample spectrum is complex, and the image sensor can only record the intensity of light, extending the sample spectrum beyond the original objective lens bandpass using the N acquired images is not direct. To solve this inverse problem, FPM applies a phase retrieval reconstruction algorithm [27, 28]. Several algorithms are available [29–31] including standard non-linear solvers based upon alternating projections, which we utilize in this work, as well as more advanced techniques [32, 33]. With careful initialization, the alternating projection algorithm arrives at the solution with high success rate despite not having convergence guarantees [5–7, 12, 13, 34]. All techniques require a certain amount of redundancy within the acquired image set. Here, we vary the LED angles such that consecutive images, which correspond to uniquely windowed areas of the sample spectrum,

#252832 Received 2 Nov 2015; revised 16 Dec 2015; accepted 29 Dec 2015; published 7 Jan 2016

overlap by approximately 65% in the Fourier domain. Independent of the algorithm, we will refer to the application of phase retrieval to expand the aperture stop bandpass as Fourier ptychographic (FP) reconstruction. In the end, we effectively increase the NA of our system by the illumination NA defined via the maximum LED illumination angle [35].

Simultaneous to complex sample reconstruction, it is also possible to use the same set of FPM images to iteratively determine the microscope's pupil function. We refer to this joint solver as EPRY [7]. The pupil function is a complex function that summarizes a microscope's aberrations in addition to its spatial frequency bandpass as a variation in amplitude and phase at its aperture plane. In an aberrated microscope, each resulting image is connected to the product of the sample spectrum (shifted laterally for an oblique LED illumination) with the same pupil function, which is nonzero only within the bandpass defined by the microscope's aperture. Using joint optimization, it is thus possible to simultaneously determine the pupil function within FP reconstruction by splitting the iterative FPM update process into two steps. First, EPRY may use the image data and current pupil function estimate to update the sample spectrum estimate at all even iterations. Then, EPRY may apply the image data and the current spectrum estimate to update the pupil function estimate at all odd iterations. A similar joint process is also used to simultaneously determine the amplitude and phase of the shifting probe field in X-ray ptychography [36–39], leading to a significant boost in solver accuracy. To account for the spatially varying aberrations across the microscope's FOV, the captured images are segmented into small tiles, for which the aberrations can be considered as spatially invariant within each tile [5, 14]. Here, we select a tile area that is smaller than the entire sample, but larger than approximately 20 x 20 sensor pixels projected onto the image plane, which helps mitigate numerical artifacts during reconstruction. The EPRY process is simply applied separately to distinct image sub-tiles. Image tiling separately considers different areas of sample and image plane, thus allowing EPRY to determine a unique aberration function from each sub-region of the microscope's FOV.

The tile-specific pupil functions obtained from the EPRY algorithm provide an accurate physical model of the microscope's coherent transfer function, as detailed in Appendix A, which means that one can also deduce from the pupil functions a correct aberration model for an incoherent imaging scheme. Given that both imaging modalities originate from within the same microscope at similar wavelengths and assuming no inter-image movement, the fluorescence image PSF is simply given by the squared magnitude of the Fourier transform of the pupil function [40]:

$$h_m(x,y) = \left| \mathcal{F}^{-1}\left[P_m(f_x, f_y) \right] \right|^2 , \tag{1}$$

where (x, y) represent the spatial coordinates of the image plane, (f_x, f_y) represent the coordinates in the aperture plane (i.e., are the Fourier conjugates of the spatial coordinates), $h_m(x, y)$ is the incoherent PSF, $P_m(f_x, f_y)$ is the CTF, and $\mathcal{F}^{-1}$ represents an inverse Fourier transform operation.

Our goal is to use this information to remove the aberrations from the fluorescence image. We segment the fluorescence image into the same sub-tiles as in the FPM reconstruction process to ensure the aberration map acquired from EPRY corresponds to the same sub-regions in the fluorescence image. We represent one tile of the fluorescent sample as $o_m(x, y)$, where *m* stands for the m^{th} tile. When $o_m(x, y)$ is imaged by an optical system, it is degraded by the possibly spatially variant incoherent PSF, $h_m(x, y)$, before reaching the detector. The detected image intensity, $i_m(x, y)$, is further corrupted by noise, $n_m(x, y)$, originating from the sample's background signal, shot noise, and detector noise [41]. The imaging process can be represented as:

#252832 Received 2 Nov 2015; revised 16 Dec 2015; accepted 29 Dec 2015; published 7 Jan 2016

$$i_m(x,y) = h_m(x,y) * o_m(x,y) + n_m(x,y). \quad (2)$$

The goal of the aberration removal in fluorescence imaging is to recover the object $o_m(x,y)$ from the corrupted image signal, $i_m(x,y)$. In the Fourier domain, Eq. (2) is represented as follows:

$$I_m(f_x,f_y) = H_m(f_x,f_y)\cdot O_m(f_x,f_y) + N_m(f_x,f_y), \quad (3)$$

where $I_m(f_x,f_y)$, $H_m(f_x,f_y)$, $O_m(f_x,f_y)$, and $N_m(f_x,f_y)$ are the Fourier transforms of $i_m(x,y)$, $h_m(x,y)$, $o_m(x,y)$, and $n_m(x,y)$, respectively. Inverting Eq. (3) to solve for $O_m(f_x,f_y)$ is an ill-posed problem due to the nature of $H_m(f_x,f_y)$, also known as the optical transfer function (OTF). Unlike the coherent transfer function, the OTF can have numerous zeros within its bandpass and its values are very low near the bandpass's edges [40], which means that the sample information is lost or overwhelmed by noise at these spatial frequencies. Various inversion methods have been developed to account for this information loss, which typically rely upon regularization parameters [42]. Wiener deconvolution [43] is one method that attempts to determine an estimate, $\tilde{O}_m(f_x,f_y)$, for the original object signal, $O_m(f_x,f_y)$, by the following:

$$\tilde{O}_m(f_x,f_y) = G_m(f_x,f_y)\cdot I_m(f_x,f_y), \quad (4)$$

where $G_m(f_x,f_y)$ is an inverse filter defined as:

$$G_m(f_x,f_y) = \frac{H_m^*(f_x,f_y)}{\left|H_m(f_x,f_y)\right|^2 + \frac{\left|N_m(f_x,f_y)\right|^2}{\left|O_m(f_x,f_y)\right|^2}}. \quad (5)$$

While it is reasonable to assume $N_m(f_x,f_y)$ is flat white Gaussian noise, $O_m(f_x,f_y)$ is hard to determine unless we have some prior knowledge of the sample's spatial distribution. For simplicity, we set $\left|N_m(f_x,f_y)\right|^2 / \left|O_m(f_x,f_y)\right|^2$ to a constant K [41, 44], essentially converting $G_m(f_x,f_y)$ to a Tikhonov regularization algorithm [45]. K acts like a regularizer: a smaller K produces sharper details while amplifying noise in the captured image whereas a larger K makes the algorithm more robust to noise at the expense of details. This value is determined visually so that the deconvolution minimizes the background noise while recovering the most detail in the final image [44]. In the end, our final estimate of the original fluorescent object is given by:

$$\tilde{o}_m(x,y) = \mathcal{F}^{-1}\left[\frac{H_m^*(f_x,f_y)}{\left|H_m(f_x,f_y)\right|^2 + K}\cdot I_m(f_x,f_y)\right]. \quad (6)$$

Equation (6) outputs the resulting image after Tikhonov regularization with our assumed noise and sample distribution model. Gaussian noise is a reasonable assumption for the noise in our system because we capture images with long exposures for high signal-to-noise ratio. However, for photon-limited settings where Poisson noise becomes severe and dominant, maximum likelihood deconvolution methods that assume a Poisson imaging process would be more suitable, such as Richardson-Lucy deconvolution [46]. We apply Eq. (6) for all the sub-tiles to acquire a full FOV aberration-corrected fluorescence image.

#252832 Received 2 Nov 2015; revised 16 Dec 2015; accepted 29 Dec 2015; published 7 Jan 2016

3. Experimental demonstration on fluorescent microspheres sample

To experimentally demonstrate both FPM and fluorescence image enhancement, we use the modified 4f setup diagrammed in Fig. 1. Here, the 4f arrangement consists of an f = 200 mm tube lens (ITL200, Thorlabs) and an f = 50 mm Nikon lens (f/1.8D AF Nikkor). We also place an iris at the back-focal plane of the f = 50 mm lens, as shown in Fig. 1, to allow for a user-controllable NA. The 4f setup has an NA of $NA_{collection}$ = 0.085 with an M = 3.87 magnification. The sample is placed at the front focal plane of the f = 50 mm lens, and a CCD detector (pixel size 5.5 μm, Prosilica GX6600) is used to capture each image. It is able to capture an area of 6.2 mm by 9.3 mm on the sample plane, defined by the detector's sensor size in this setup. The setup includes two illumination sources, one for each imaging modality. For high-resolution FPM imaging, we use an LED array placed ~80 mm behind the sample with 32x32 individually addressable elements (pitch size 4 mm), of which we only use a 15x15 segment (225 images captured in total). The increase in NA provided by the LEDs is NA_{illum} = 0.33. The overall system NA is $NA_{sys} = NA_{collection} + NA_{illum}$ = 0.33 + 0.085 = 0.415, which is a factor of 4.9 resolution gain over the 4f setup with a single plane wave illumination. For fluorescence imaging, we use a separate excitation LED along with an appropriate emission filter that we insert in the optical path behind the iris. FPM raw images and the fluorescence image are captured separately. The emission filter is present only for capturing the fluorescence image and the FPM raw images of the same color channel, which ensures they both image the same spectral range.

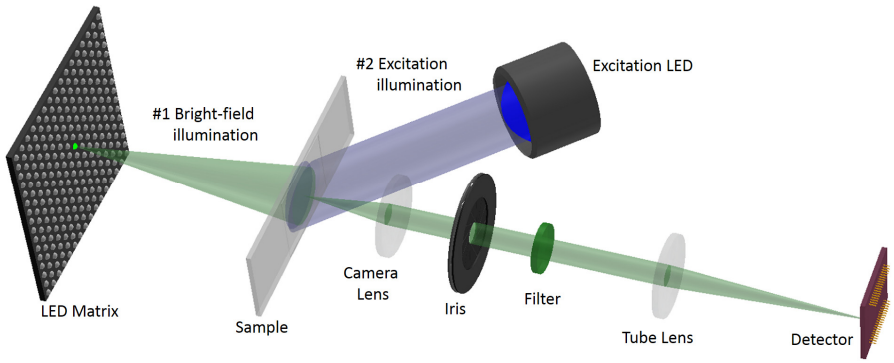

Fig. 1. The experimental setup of joint FPM-fluorescence imaging. The 4f setup has a camera lens, an iris at the back focal plane, and a tube lens. The filter is included only for fluorescence imaging and FPM imaging of the same color channel. First, raw FPM images are captured using varied-angle illumination provided by the LED matrix. Then, a fluorescence image is captured with the illumination from the excitation LED.

As a first experimental demonstration of our algorithm pipeline, we image a sample slide containing both 10 μm green-fluorescing microspheres and 15 μm non-fluorescing microspheres (Fisher Scientific). First, we acquire 225 full FOV low-resolution images under variable LED illumination (< 3 seconds average exposure time). Only green LEDs are used for this demonstration. We focus our attention on a single image tile in Fig. 2, which corresponds to a 360 μm x 360 μm region located 3.8 mm away from the center of the image FOV. From our set of 225 low-resolution images captured under variable green LED illumination (in Fig. 2(a)), we apply the EPRY algorithm for 50 iterations (5 seconds per tile) to reconstruct the intensity and phase of the sample, along with the pupil function of the optical system (in Fig. 2(b)). Note, this pupil function is only valid for this particular image tile, and the reconstructed complex image is much sharper than the raw images due to resolution improvement and aberration removal. Next, we capture a green fluorescence image by illuminating the sample with our blue excitation LED (470 nm, Thorlabs), in Fig. 2(c) (2 minutes exposure time). Both FPM images and the fluorescence image are captured using a

#252832 Received 2 Nov 2015; revised 16 Dec 2015; accepted 29 Dec 2015; published 7 Jan 2016

green band-pass filter (530 nm, 43 nm pass band) behind the iris. The fluorescence image is severely blurred because it is captured near the edge of the imaging system's FOV. We can derive the incoherent PSF that characterizes the fluorescence image blur, $h_m(x,y)$, from the EPRY algorithm's computed pupil function, $P_m(f_x,f_y)$, following Eq. (1).

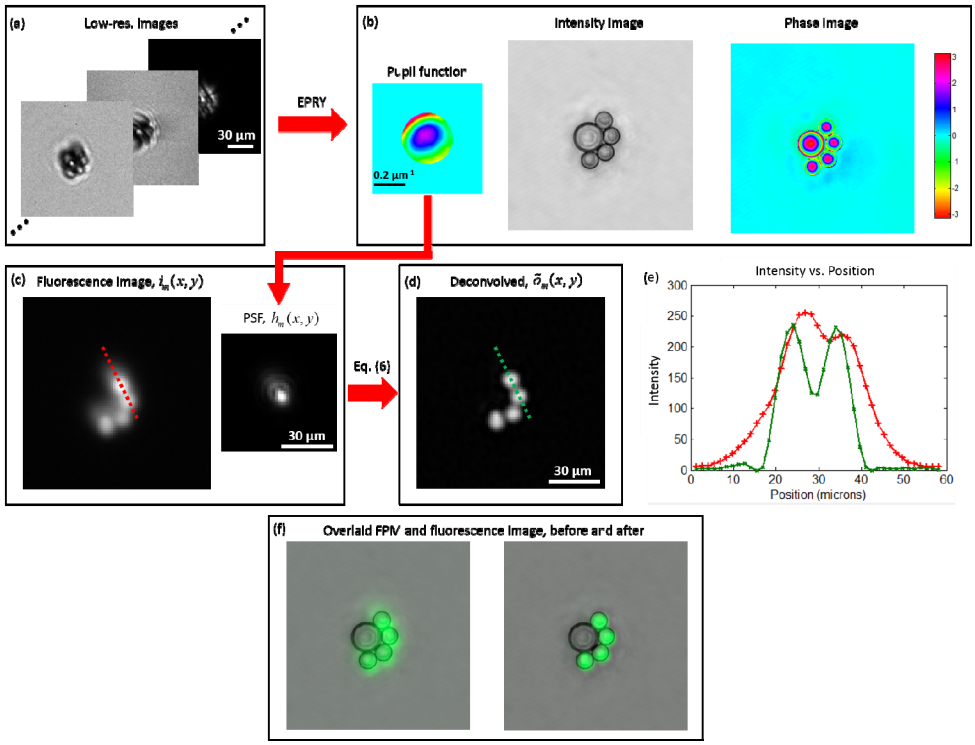

Fig. 2. Experimental reconstruction of an improved-resolution amplitude and phase image, along with an aberration-corrected fluorescence image, using FPM. (a) Series of low-resolution coherent green images captured with variable-angle illumination from an LED matrix. (b) EPRY is applied on the low-resolution images to generate a high-resolution, complex image of the sample, along with the characterization of the microscope's pupil function. (c) The pupil function is converted into an incoherent PSF, which is the blur kernel induced to a fluorescence image by the imaging system in the same sample region. (d) The PSF is deconvolved from the fluorescence image using Eq. (6) to generate an aberration-corrected image. (e) The one-dimensional profile of two beads, in the raw and deconvolved images, shows improved contrast and position accuracy. (f) In the overlay of FPM and fluorescence images, the fluorescence signal is localized with good centroid accuracy after deconvolution.

We then deconvolve the PSF-induced blur from our fluorescence image in Fig. 2(c) using Eq. (6), which creates the sharp image in Fig. 2(d) (< 1 second per tile). Deconvolution removes many of the negative effects of lens-induced aberration. Four fluorescent beads that are challenging to resolve in the raw image are clearly distinguishable after deconvolution. In Fig. 2(e), we plot the one dimensional profile through two neighboring beads, both with raw and deconvolved data. This plot highlights that not only does our deconvolution improve image contrast, but it also locates the centroid of each bead with greater accuracy. Specifically, the ratio of the lower peak to the dip between each peak is 0.946 for the raw image and 0.526 for the deconvolved result. The raw image shows the beads' separation distance is 8.5 μm, which is 15% below the bead's diameter of 10 μm. The deconvolved image shows the separation of 9.9 μm, which is within the 5% tolerance value indicated within the beads' manufacturing specifications. We also note that the lateral shift caused by the system's aberrations is corrected for in the deconvolution result, as indicated by the shift

#252832 Received 2 Nov 2015; revised 16 Dec 2015; accepted 29 Dec 2015; published 7 Jan 2016

of the inter-peak dip. This is important for identifying the correct spatial correspondence between the high-resolution FPM image and the fluorescent sample image.

4. FPM and fluorescence imaging of HeLa cells

To demonstrate the benefit of combined bright-field and fluorescence imaging with a biological sample, we use our system to image a sample of HeLa cells stained for both fluorescence and bright-field. The sample is a microscope slide with 90% confluent HeLa cells that are fixed, stained with Wright's stain from Fisher Scientific's PROTOCOL Hema 3, and fluorescently tagged with DAPI from Life Technologies. The sample is first imaged for FPM reconstruction by sequentially illuminating it with the red, green, and blue channels of the 225 LEDs in our array. We insert a bandpass filter (460 nm, 80 nm band) to capture blue illumination images from within the same spectral range as DAPI's fluorescence emission. Second, we capture a blue fluorescence image by illuminating the sample with a UV LED (365 nm, Thorlabs) at DAPI's excitation wavelength. The sample is exposed for 21 minutes, which is the optimal time for the given sample and imaging setup as detailed in Section 5. We then reconstruct a high-resolution FPM image, along with a spatially varying pupil function, by repeating the EPRY algorithm on different image sub-tiles. Finally, we apply Eq. (6) to deconvolve each tile of the fluorescence image.

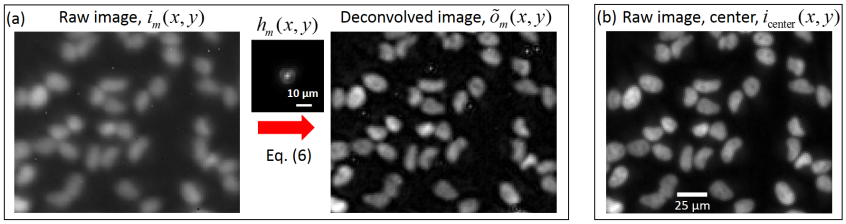

Fig. 3. Comparison between (a) a raw image of a specific sample ROI shifted 4.63 mm off the optical axis (left), its deconvolution result (right), and (b) a raw image captured with the same sample ROI centered on the optical axis, $i_m(x,y)$. The PSF recovered from FPM, $h_m(x,y)$, is deconvolved from the image to remove aberrations in (a). The result shows close resemblance to the image in (b), $i_{center}(x,y)$, which we assume is minimally impacted by system aberrations.

As a qualitative performance test of our deconvolution, we capture two fluorescence images of the same sample region of interest (ROI), shifted to two different locations within the optical system's FOV. We capture one image with the ROI located at the center of the image FOV (i.e., along the optical axis, shown in Fig. 3(b)). In this region, we assume the effects of imaging system aberrations are minimal and treat this image as the ground truth for comparison. We could deconvolve this image with the associated PSF, which could potentially improve the image contrast. However, the result of Tikhonov regularization can at best only be an estimate of the true sample function, as given by the assumption on K in Eq. (6). Therefore, we do not perform deconvolution on the center image. We then capture a second image of the same ROI after translating the sample laterally 4.63 mm away from the center, as shown in Fig. 3(a). It is clear that lens aberrations more significantly impact image quality off the optical axis, as indicated by the blurry outlines of the DAPI-stained nuclei. The same sub-figure also shows the results of our deconvolution, using the incoherent PSF found via FPM image capture and post-processing of the same image tile. Deconvolution both increases the nuclei's contrast and highlights features that are not otherwise visible in the raw fluorescence image to the left, such as the shape of the nuclei and their separation gaps. We can confirm the accuracy of our deconvolution result in Fig. 3(a) by comparing it with the minimally aberrated image of the same ROI in Fig. 3(b). We see close agreement between all deconvolved image features, with few apparent artifacts. Some "hot" pixels, visible as white or black dots within the raw, blurry image in Fig. 3(a), lead to ringing artifacts around each

#252832 Received 2 Nov 2015; revised 16 Dec 2015; accepted 29 Dec 2015; published 7 Jan 2016

after deconvolution. However, their presence does not drastically degrade the quality of the deconvolution image.

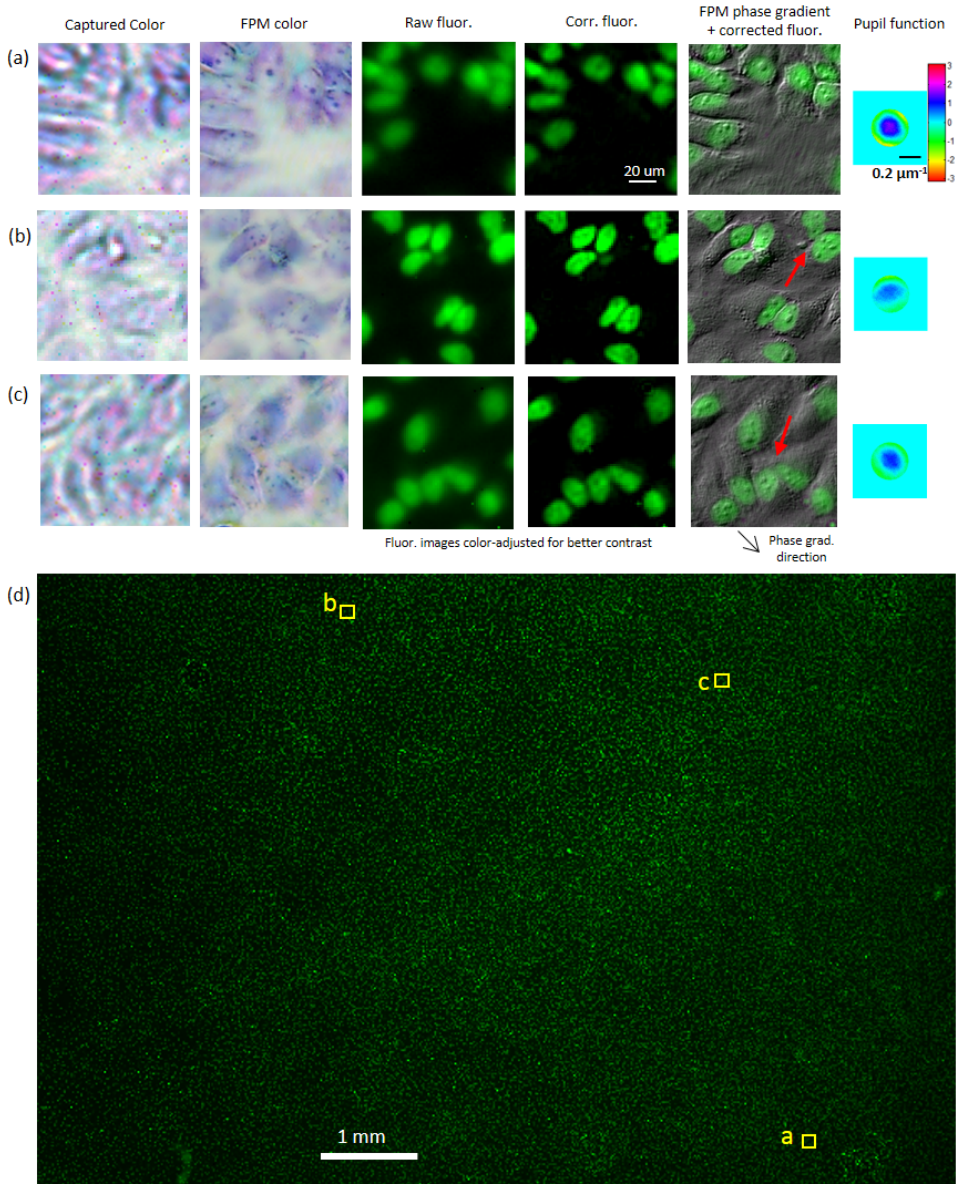

Fig. 4. Demonstration of FPM and aberration-corrected fluorescence imaging across different regions of a large image FOV. (a)-(c) correspond to regions labeled in the full FOV fluorescence image in (d). With FPM, we improve bright-field image resolution (1st and 2nd column) and characterize the spatially varying pupil functions (6th column). Hot pixels and chromatic aberrations appearing in the low-resolution color images are suppressed and corrected after FPM reconstruction. We correct aberrations in the fluorescence image using each pupil function (3rd and 4th column). The phase gradient images from FPM can be combined with fluorescence data to elucidate the structures and the locations of the nuclei of HeLa cells (5th column). The cell membrane morphology elucidated by the phase gradient can differentiate between cells undergoing cytokinesis (arrow in (b)) and cells in telophase (arrow in (c)), which is otherwise difficult to do in the fluorescence images alone.

#252832 Received 2 Nov 2015; revised 16 Dec 2015; accepted 29 Dec 2015; published 7 Jan 2016

Figure 4 offers an example of combining both our resolution-improved bright-field imaging and fluorescence imaging capabilities within a single biological application. Here, similar to Fig. 3, we process low-resolution images obtained under variable-LED illumination using the EPRY algorithm. Prior to reconstruction, the low-resolution color images have severe aberrations because they are captured near the edge of the FOV. We can reconstruct high-resolution, aberration-corrected full-color FPM images to elucidate sharp image features, such as the nucleoli present in the HeLa cells' nuclei, cell morphology via the reconstructed phase, and boundaries between different cells. Figure 4(d) is the full FOV fluorescence image of the HeLa sample, and Figs. 4(a)-4(c) correspond to zoomed-in regions of the image to demonstrate that we are able to obtain high resolution FPM images and aberration-corrected fluorescence images throughout the entire image FOV. Generating a full FOV image requires applying EPRY and deconvolution algorithms to individual subtiles separately (~2200 tiles, 5 seconds per tile). We can also combine the fluorescence image with FPM data to generate a phase gradient image overlaid with fluorescence emission. The phase gradient + fluorescence images in Figs. 4(a)-4(c) show that, with the help of the cell's structural information provided through the phase gradient, the fluorescent regions of HeLa cells are indeed the nuclei. It is also possible to distinguish cells in telophase (Fig. 4(c) arrow) from the ones in the cytokinesis stage of cell mitosis (Fig. 4(b) arrow), by examining the cell membrane morphology within the phase gradient image. This type of information is missing from fluorescence data alone. It is important to note that, because the aberrations in FPM and fluorescence imaging are corrected by functions derived from the same pupil function, we also observe accurate spatial correspondence (i.e., alignment) between each imaging modality.

5. Quantifying the adequate amount of fluorescence signal for deconvolution

We observe that the quality of our deconvolution results is proportional to the signal-to-noise ratio (SNR) of the input images. As noted previously, Eq. (6) is based on Gaussian noise model; thus, applying it on an image dominated by Poisson noise will not result in successful deconvolution. It is important to investigate at what SNR level our method can start yielding accurate deconvolved images. Although we can image the DAPI fluorescence dye (used to stain our HeLa cells in Fig. 3 and Fig. 4) for an extended period of time without photobleaching to obtain a high SNR, many fluorescence dyes are not as robust [1, 3]. For a weakly fluorescing sample (e.g. low fluorophore concentration), one needs to extend the detector exposure time and runs into the risk of photobleaching the sample before the end of an image capturing process. Thus, the system's parameters need to be adjusted appropriately to image the sample before photobleaching occurs. Also, to our knowledge, this is the first published work to demonstrate deconvolution of fluorescence images with the aberration function derived from an iterative computational method using coherent microscopy. All aforementioned reasons prompted us to conduct further analysis on our deconvolution method. In the following paragraphs, we systematically analyze how an imaging system's parameters play a role in the fluorescence image capturing process and quantify how much fluorescence signal is required for our system to offer good deconvolution results.

In a CCD detector, photons hitting the sensor generate electrons in each pixel. In the readout process, the number of electrons are converted into a discrete photon count value, S, by a gain factor, g. S includes various kinds of noise, σ_s, such as dark current, read noise, quantization noise, and shot noise [47]. The per-pixel SNR is then given by:

$$\mathrm{SNR} = \frac{S}{\sigma_s}. \tag{7}$$

We assume shot noise, which originates from the quantum nature of light, to be the dominant noise and ignore others for simplicity of our analysis. Further assuming our CCD's

#252832 Received 2 Nov 2015; revised 16 Dec 2015; accepted 29 Dec 2015; published 7 Jan 2016

gain to be $g = 1$, S is directly related to σ_s by: $\sigma_s = \sqrt{\langle S \rangle}$ [47], where $\langle S \rangle$ is the average pixel count. Thus, SNR increases with an increase in signal value (i.e. SNR = $S/\sqrt{\langle S \rangle}$).

To determine a threshold SNR of fluorescence signal needed for successful deconvolution, we capture multiple fluorescence images of the region in Fig. 3 (i.e. 4.63mm away from center), each with a different exposure time. An increase in exposure time leads to an increase in S registered by our detector's pixels for the fluorescent nuclei of HeLa cells. Since each HeLa nucleus has a different fluorescence signal level due to different amount of bound DAPI molecules, we select one representative HeLa nucleus within the ROI for quantifying signals in this study. Specifically, we use a small uniform region within the nucleus, as indicated by the yellow box in Fig. 5(b), to calculate average SNR values. As we vary the exposure time, t, from 45 seconds to 37.5 minutes, SNR varies from 3.46 to 24.16. We then deconvolve each variable exposure image $i_m(\mathbf{u};t)$ via Eq. (6) with the same deconvolution filter to create a set of sharpened reconstructions, $\tilde{o}_m(\mathbf{u};t)$. We compare each of these sharpened images to a reference image, $i_{\text{center}}(\mathbf{u})$, created again by centering the same image ROI along the optical axis. We assume this centered image is a minimally aberrated, and thus a useful comparison benchmark. It has a much greater SNR (SNR = 41.14) compared to the off-center images. Note that $\tilde{o}_m(\mathbf{u};t)$ is the estimate of the sample function, $o_m(\mathbf{u})$, and $i_{\text{center}}(\mathbf{u})$ is the convolution of $o_m(\mathbf{u})$ with the incoherent PSF of the center FOV (which is only minimally aberrated), $h_{\text{center}}(\mathbf{u})$, as given by Eq. (2) (assuming $n_{\text{center}}(\mathbf{u}) \approx 0$ for a high SNR). We do not apply Tikhonov regularization to $i_{\text{center}}(\mathbf{u})$ to obtain $\tilde{o}_{center}(\mathbf{u})$ because $\tilde{o}_{center}(\mathbf{u})$ would at best only be an estimation for the true sample function $o_m(\mathbf{u})$, especially without the knowledge of the sample's spatial frequency distribution, $O_m(f_x, f_y)$, and the exact noise distribution, $N_m(f_x, f_y)$, as indicated in Eq. (5). Thus, we treat $i_{\text{center}}(\mathbf{u})$ as the ground truth in our analysis. In order to quantify the accuracy of $\tilde{o}_m(\mathbf{u};t)$, we convolve $\tilde{o}_m(\mathbf{u};t)$ with $h_{\text{center}}(\mathbf{u})$ to generate $\tilde{i}_m(\mathbf{u};t)$ for appropriate quantitative comparison between the estimated and the ground truth sample function. We then compare each $\tilde{i}_m(\mathbf{u};t)$ with $i_{\text{center}}(\mathbf{u})$ by computing their normalized mean square error (NMSE) [48], which is a function of exposure time, t:

$$\text{NMSE}(t) = \frac{\sum_{\mathbf{u}} \left| i_{\text{center}}(\mathbf{u}) - \alpha_t \tilde{i}_m(\mathbf{u};t) \right|^2}{\sum_{\mathbf{u}} \left| i_{\text{center}}(\mathbf{u}) \right|^2}. \tag{8}$$

Here, $\mathbf{u} = (x, y)$, and α_t is given by:

$$\alpha_t = \frac{\sum_{\mathbf{u}} i_{\text{center}}(\mathbf{u}) \cdot \tilde{i}_m^{\,*}(\mathbf{u};t)}{\sum_{\mathbf{u}} \left| \tilde{i}_m(\mathbf{u};t) \right|^2}, \tag{9}$$

which allows for NMSE metric to be invariant to a constant multiplicative factor between images being compared.

For a quantitative validation of the improvement in image quality after our deconvolution algorithm, we also calculate the NMSE between the raw away-from-center images, $i_m(\mathbf{u};t)$, and the reference image, $i_{\text{center}}(\mathbf{u})$. As shown in Fig. 5, the deconvolved images are able to consistently provide lower NMSE values than do the raw images, with NMSE reduced by 31% in the plateau region (NMSE = 0.0057 versus 0.0087). Both plots start to plateau at about $t = 21$ min, at which the SNR in the raw captured image is SNR = 18.1. We set this as the adequate SNR value of a fluorescence image for successful deconvolution.

#252832 Received 2 Nov 2015; revised 16 Dec 2015; accepted 29 Dec 2015; published 7 Jan 2016

We then quantify how much fluorescence a sample needs to emit for our particular imaging system to obtain the adequate SNR image. This quantity can guide the sample preparation process and the imaging system setup so that the sample's bound fluorophore concentration level and the imaging system's parameters are made suitable for successful fluorescence image deconvolution. Assuming that the DAPI fluorophores in the nucleus of interest emit n photons per area isotropically (i.e. spherical wavefront from each point on the nucleus), the proportion entering our system, $n \cdot m$, with the given numerical aperture, NA, can be determined by calculating how much fraction of the spherical area is captured by the system. NA limits the light acceptance angle and results in capturing a section of the sphere, a spherical cap [49]. The ratio of the spherical cap to the total spherical area is equal to $m = (1 - \sqrt{1 - (\mathrm{NA}/n_\mathrm{i})^2})/2$, where n_i is the index of refraction of the medium between the sample and the imaging lens. For our system, $n_\mathrm{i} = 1$, so it is omitted in subsequent calculations. The photons reach our CCD detector and are converted into electrons with the conversion ratio determined by the quantum efficiency, q (q = 46% at λ = 470 nm for our system). With the magnification of our imaging system, M = 3.87, CCD gain assumed to be g = 1, and the pixel area, p = 30.25 μm^2, the output signal for a pixel is given by:

$$S = \frac{nmpq}{M} = \frac{npq(1 - \sqrt{1 - \mathrm{NA}^2})}{2M}. \tag{10}$$

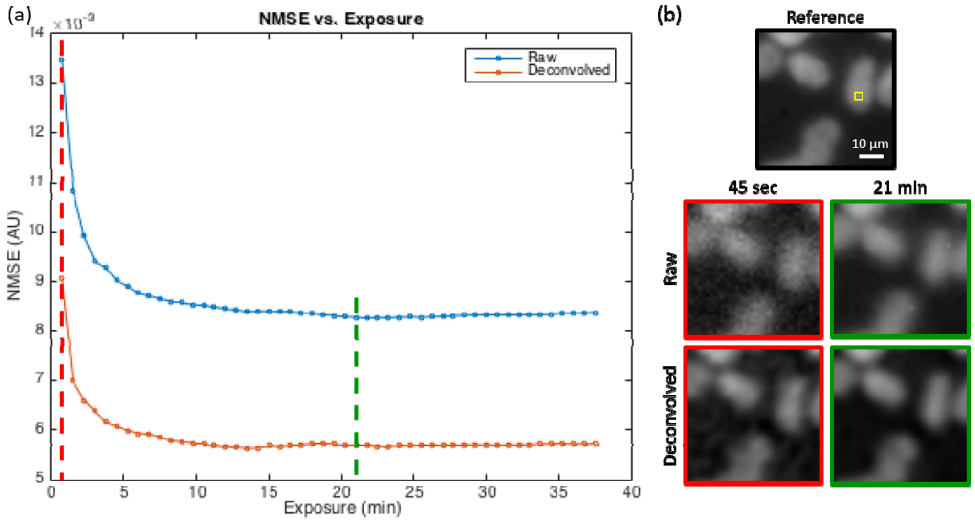

Fig. 5. (a) Normalized mean square error (NMSE) of the raw, $i_m(\mathbf{u};t)$, and deconvolved image, $\tilde{i}_m(\mathbf{u};t)$, in Fig. 3(a) is plotted against the detector exposure time. Higher exposure is equivalent to higher SNR of the captured image. NMSE starts to plateau for both raw and deconvolved images after about 21 min of exposure (raw image SNR = 18.1) as indicated by the green broken line, with the deconvolved image's NMSE = 0.0057 being 31% lower than the raw image's NMSE = 0.0083. (b) Example images of the ROI used for this study. The reference image is generated by centering the ROI and capturing with our imaging system. We use the area inside the small yellow box to quantify the SNR. Raw images are captured with varying exposure time (45 sec and 21 min shown here) while the ROI is 4.63 mm away from the center. We use the same small area in each raw image to quantify its SNR. Deconvolved images are generated by applying Eq. (6) to the raw images. Longer exposure provides better SNR images and deconvolution results.

We look at a uniform region within a HeLa nucleus, so $S = \langle S \rangle$. Thus, our average SNR is given by:

#252832 Received 2 Nov 2015; revised 16 Dec 2015; accepted 29 Dec 2015; published 7 Jan 2016

$$\mathrm{SNR} = \frac{\langle S \rangle}{\sqrt{\langle S \rangle}} = \sqrt{n}\sqrt{\frac{pq(1-\sqrt{1-\mathrm{NA}^2})}{2M}}. \tag{11}$$

Rearranging for n, we find:

$$n = \mathrm{SNR}^2 \frac{2M}{pq(1-\sqrt{1-\mathrm{NA}^2})}. \tag{12}$$

Substituting the values for our system parameters, the number of photons per area required for an adequate SNR in our system is n = 50400 photons/μm^2. This condition allows for our deconvolution algorithm to achieve an accurate result with a low NMSE value. The fluorescent sample needs to be exposed for an adequate amount of time to satisfy the n requirement. For a sample that cannot provide this much signal either due to photobleaching or restrictions on exposure time, the system parameters need to be adjusted appropriately according to Eq. (11) to achieve a similar SNR level.

6. Discussion and conclusion

In summary, we have developed an FPM system capable of generating a wide-field, aberration-corrected fluorescence image with correct spatial correspondence to the high-resolution FPM image. It utilizes the spatially varying pupil function from EPRY algorithm to correct for the aberrations in the fluorescence image. The resulting color intensity image, phase image, and the fluorescence image can be combined to provide multiple layers of information about the sample's morphology, chemical properties, and functions. The wide FOV fluorescence and high-resolution bright-field image can be beneficial to various biological imaging studies including, but not limited to, cell lineage tracing, counting bacteria, and cell migration. For imaging scenarios requiring the use of a higher NA objective lens, the same algorithm may be used with the FPM setup adjusted accordingly by simply varying the distance of the LED matrix to the sample to allow for steeper angles of illumination, as demonstrated in [35].

The advantages of this aberration-removal method with the same pupil function from FPM over other deconvolution methods are the following: 1) deconvolution by the PSF obtained from FPM allows for proper overlap between the fluorescence image and the FPM image. This is important when overlaying the two images, especially when the pupil function has large asymmetric aberrations in different regions of the FOV. Asymmetric aberrations cause a noticeable lateral shift in the images. Since the presented deconvolution method uses the incoherent PSF determined directly from the pupil function obtained from EPRY, both the fluorescence image and FPM's high-resolution coherent image can be corrected for aberrations with the same amount of lateral shift. Other deconvolution methods that do not use the pupil function characterized by FPM, such as blind deconvolution, would not be able to generate a corrected image with the proper lateral shift because the methods do not account for the absolute location of the image [50], meaning that the deconvolved image can have any arbitrary lateral shift as its solution. Without the same lateral shift for FPM and fluorescence images, the direct overlay of the images will not have the correct spatial correspondence between them. 2) Because the system can characterize the PSF of the fluorescence image, one can refer to the vast amount of literatures on non-blind deconvolution methods to deconvolve the aberrations from the image. Various high-fidelity and noise-robust methods, such as [51, 52], can be implemented once the PSF is known. 3) The aberration correction method can be easily implemented in other fluorescence imaging setups since the pupil characterization by FPM only requires an attachment of an LED matrix to the existing microscope setup. For example, the recent development of the pattern-illumination Fourier ptychography for high-resolution fluorescence imaging [15] can benefit from the aberration correction of the fluorescence images prior to the reconstruction process because the technique does not correct

#252832 Received 2 Nov 2015; revised 16 Dec 2015; accepted 29 Dec 2015; published 7 Jan 2016

for spatially varying aberrations during the reconstruction. The addition of our aberration-correction method to the system will enable high-resolution, wide-field fluorescence imaging that can complement the coherent FPM imaging at a more comparable resolution scale.

One major disadvantage of this fluorescence imaging schematic is that the setup can only work for thin samples. It cannot do sectioning of thick samples (e.g., unlike confocal microscopy and light sheet microscopy) because FPM currently only works in the thin sample regime [35]. The regime corresponds to ~4.5 μm given our system's parameters, which is suitable for imaging HeLa cells, which are about 2 μm thick [53]. If there are fluorescence signals on multiple layers of the sample or if the sample is thick, the system will not be able to properly characterize the pupil function and correct the images. For multi-layer samples, the multi-slice FPM approach [54] is a possible solution for this problem. Another minor disadvantage of our schematic is that we are only able to correct for red, green, and blue fluorescence signals due to the limited number of color channels in our LED matrix. This can be addressed by using broad-spectrum LEDs or other light sources and inserting appropriate band-pass filters of desired wavelengths for acquiring FPM images. Fluorescence of various wavelengths can then be corrected with the aberration maps characterized at respective wavelengths.

Appendix A: crosschecking EPRY with an alternative pupil recovery method

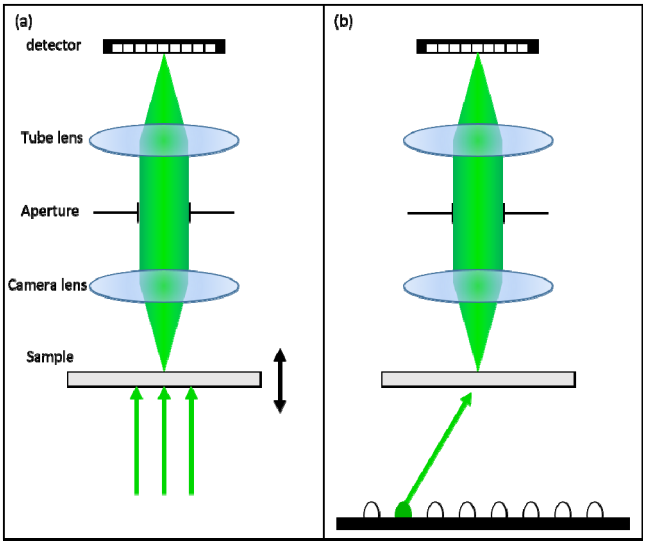

Fig. 6. The variations in experimental setup for comparing the two different pupil function recover methods. (a) Collimated light source illuminates the sample perpendicularly, and the sample is brought to different defocus planes in the defocus diversity-based pupil recovery method. (b) LEDs of varied illumination angles act as the light source in FPM setup. EPRY algorithm jointly solves for the sample spectrum and the pupil function using sample images captured under different LED illumination angles.

It is necessary to verify that EPRY is able to recover a physically accurate model of the microscope's pupil function. Although [7] shows that EPRY algorithm converges to the actual pupil function in computer simulations, it only demonstrates the algorithm's robustness in experiments via visual inspection of reconstructed sample images. Here, we proceed to confirm that it converges to the correct pupil function in real imaging situations by comparing the generated pupil function with that obtained from another pupil function recovery method. We crosscheck EPRY with an alternative method capable of characterizing spatially varying aberrations of an imaging system as described in [14]. Its principle is based on a phase-retrieval technique on a sample via phase diversity introduced by imaging the sample at various defocus planes [55–57]. The basic procedure is as follows. The sample has identical

#252832 Received 2 Nov 2015; revised 16 Dec 2015; accepted 29 Dec 2015; published 7 Jan 2016

targets, such as microspheres, distributed uniformly across the imaging FOV. A target at the center of the FOV is considered to be minimally aberrated by the imaging system. Its complex function obtained via the phase retrieval technique is therefore treated as the ground truth of the target's complex field. The aberration function of any region of the imaging system's FOV can be recovered using the defocus image stack of a target in that certain area and the target's ground truth. The aberration function with a given number of parameters can be optimized for those parameters with a pattern search algorithm by minimizing the difference between the measured defocus image stack and a simulated defocus stack. The latter is generated by applying the aberration function on the ground truth target and propagating at the same defocus planes as the measured stack. The aberration function that minimizes the difference provides an accurate description of the pupil function in that region of the imaging system's FOV.

For an experimental implementation of this method, we use the same modified 4f setup diagrammed in Fig. 1 without the excitation LED. We replace the LED array with a collimated green LED beam to illuminate the sample at a perpendicular angle for this procedure, as shown in Fig. 6(a).

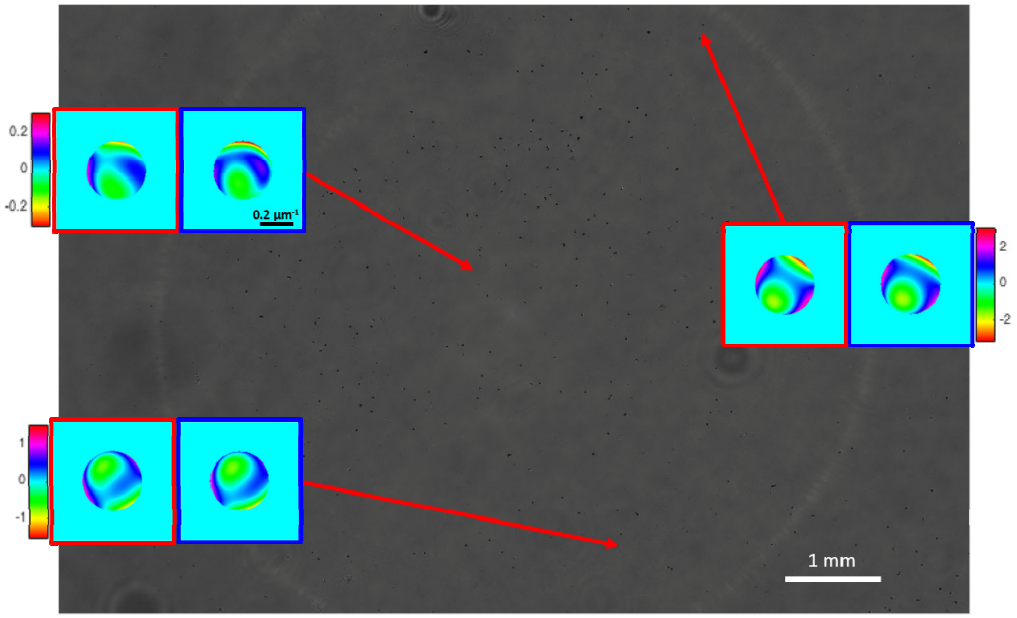

Fig. 7. Full FOV image of a sample of microspheres with associated pupil functions in 3 different sub-regions. The red box indicates the pupil function recovered by EPRY while the blue box stands for defocus diversity-based pupil function recovery method. The two pupil estimation methods correlate well throughout different regions of the FOV.

We use a microscope slide sample consisting of uniformly distributed 3 μm and 15 μm diameter microspheres (Fisher Scientific) immersed in oil and sealed with a coverslip as our target. The sample is brought to 17 different defocus planes, Δz away from the focal plane of the microscope, where Δz ranges from –400 μm to +400 μm with 50 μm steps. We select a 3 μm diameter bead at the center of the microscope's FOV as the ground truth and apply the defocus diversity phase retrieval process to obtain its complex function. We choose one 3 μm bead from different regions in the microscope's FOV, and apply the aforementioned pattern search optimization algorithm to determine the pupil functions in those regions. We optimize the pupil functions for 8 parameters corresponding to the first, second, third, and fourth order Zernike modes, which are namely x-tilt, y-tilt, x-astigmatism, y-astigmatism, defocus, x-coma, y-coma, and spherical aberration.

#252832 Received 2 Nov 2015; revised 16 Dec 2015; accepted 29 Dec 2015; published 7 Jan 2016

The experimental setup for EPRY is as follows. The setup is identical as above except for a 32x32 individually addressable RGB LED array (4 mm pitch) replacing the collimated light source, as shown in Fig. 6(b). We place the LED array ~80 mm below the sample, and use a 15x15 segment in the acquisition process (225 images captured in total). Only green LEDs were used for this procedure. We segment the full FOV into sub-tiles, and reconstruct both the pupil function and the high-resolution sample function specific to each tile. In agreement with our assumption, the central FOV shows minimal aberrations. For accurate comparisons between the two aberration characterization methods, we normalize all the pupil functions obtained by EPRY by the center tile's pupil function. We compare these to the pupil functions in corresponding regions obtained from the defocus diversity method, of which 3 pairs are plotted in Fig. 7. We only include the second, third, and fourth order Zernike modes in this comparison. The first order Zernike modes, namely the x-tilt and y-tilt, merely produce lateral shifts in a captured image, so they are not considered as aberrations.

We observe that the recovered pupil functions from the two methods correlate well across the FOV. Slight discrepancies can be attributed to imperfections in the collimation of LED and misalignment between the sample's defocus axis and the microscope's optical axis in Fig. 6(a)'s setup. We conclude that the pupil function generated by EPRY is an accurate physical description of the imaging system, which can be subsequently appropriated for fluorescence imaging.

Acknowledgments

This project was funded by the National Institute of Health (NIH) Agency Award: R01 AI096226; and the Caltech Innovation Initiative (CII): 25570015. We thank Mooseok Jang for helpful discussions.

#252832 Received 2 Nov 2015; revised 16 Dec 2015; accepted 29 Dec 2015; published 7 Jan 2016